PCCP

PAPER

Cite this: *Phys. Chem. Chem. Phys.*, 2017, **19**, 20677

Ultra low lattice thermal conductivity and high carrier mobility of monolayer SnS_2 and $SnSe_2$: a first principles study

Aamir Shafique, Abdus Samad and Young-Han Shin *

Received 4th June 2017,
Accepted 14th July 2017

DOI: 10.1039/c7cp03748a

rsc.li/pccp

Using density functional theory, we systematically investigate the lattice thermal conductivity and carrier mobility of monolayer SnX_2 (X = S, Se). The room-temperature ultra low lattice thermal conductivities found in monolayer SnS_2 (6.41 W m^{-1} K^{-1}) and $SnSe_2$ (3.82 W m^{-1} K^{-1}) are attributed to the low phonon velocity, low Debye temperature, weak bonding interactions, and strong anharmonicity in monolayer SnX_2. The predicted values of lattice thermal conductivity are lower than those of other two-dimensional materials such as stanene, phosphorene, monolayer MoS_2, and bulk SnX_2. High phonon-limited carrier mobilities are obtained for the monolayer SnX_2. For example, the electron mobility of monolayer SnS_2 is 756.60 cm^2 V^{-1} s^{-1} and the hole mobility is 187.44 cm^2 V^{-1} s^{-1}. The electron mobility of these monolayers is higher than their hole mobility due to the low effective mass of electrons and low deformation constants, which makes them n-type materials. Due to their ultra low lattice thermal conductivities coupled with high carrier mobilities, monolayer SnX_2 materials may be promising materials for thermoelectric applications.

1 Introduction

After the exploration of graphene, the search for new two-dimensional materials started both for fundamental research and device applications in the field of optoelectronics and energy conversion and storage.[1–4] Monolayer MoS_2-like transition metal dichalcogenides have gained tremendous interest due to their variety in band gaps, mechanical and chemical properties, and applications in thin film solar cells, metal ion batteries, and thermoelectric devices.[5–10] Thermoelectric materials convert waste heat energy directly into useful electrical energy. The thermoelectric performance of a material is scaled in terms of figure of merit (ZT), defined as $ZT = \frac{\alpha^2 \sigma T}{\kappa_e + \kappa_l}$, where α is the Seebeck coefficient, σ is the electrical conductivity, T is the absolute temperature, κ_e is the electronic thermal conductivity, and κ_l is the lattice thermal conductivity.[11,12] This definition recommends materials having low lattice thermal conductivity and high carrier mobility for efficient thermoelectrics.

One of the crucial problems in thermoelectric materials is the high lattice thermal conductivity which decreases the ZT. Materials having low lattice thermal conductivity are more significant in thermoelectrics. Since the electronic thermal conductivity has a direct dependence on the electrical conductivity, reducing the electronic thermal conductivity by reducing the electrical conductivity is not an effective method. According to Slack's theory of nonmetallic crystals, the requirements for low lattice thermal conductivity are strong anharmonicity (large Grüneisen parameters), weak interatomic bonding interactions, structural complexity, and materials containing heavy elements.[13] For example, because of the high lattice thermal conductivity (2200 W m^{-1} K^{-1}) of graphene, its use in thermoelectric devices is not attractive.[14] On the other hand, several two-dimensional materials like stanene, silicene, phosphorene, MoS_2, $MoSe_2$, WSe_2, SnSe, and Bi have been reported for low lattice thermal conductivities at room temperature.[15–22]

In semiconductor devices, the carrier mobility by holes and electrons plays an important role. The lattice thermal conductivity can be reduced by producing vacancies or doping heavy elements, but they decrease the carrier mobility as well. However, high carrier mobility coupled with low lattice thermal conductivity is required for efficient thermoelectric materials. Graphene, phosphorene, silicene, and monolayer MoS_2, TiS_3, SnSe, GeS, PbS, and PbSe have been reported to have high carrier mobility.[23–27] Monolayer SnX_2 (X = S, Se) have been recently synthesized and their structural parameters and electronic band structures are well studied.[28] Several recent reports show that the bulk SnX_2 has very low lattice thermal conductivity,[29,30] but the lack of research into the lattice thermal conductivity and carrier mobility of their monolayer phases motivated us to study them. Since these monolayers contain heavy elements such as Sn and

Department of Physics, University of Ulsan, Ulsan 44610, Republic of Korea. E-mail: hoponpop@ulsan.ac.kr; Fax: +82 52 259 1693; Tel: +82 52 259 1027

Se with weak interatomic bonding, it is expected that these materials will have low lattice thermal conductivity.

This paper explores the phonon transport properties such as phonon dispersion, phonon group velocities, Grüneisen parameters, lattice thermal conductivities, and phonon-limited carrier mobilities of the monolayer SnX_2, using the phonon Boltzmann transport equation and deformation potential theory. It is found that the lattice thermal conductivity of monolayer $SnSe_2$ at room temperature is as low as 3.82 W m^{-1} K^{-1}, which is attributed to the heavy atomic masses of Sn and Se and its strong phonon anharmonicity. The calculated lattice thermal conductivities are lower than the in-plane lattice thermal conductivity of their bulk phases unlike in MoS_2 and $MoSe_2$.[31,32] The carrier mobility of the monolayer SnS_2 at room temperature is as high as 756.60 cm^2 V^{-1} s^{-1} for electrons and 187.44 cm^2 V^{-1} s^{-1} for holes. The contribution of each mode to the lattice thermal conductivity is evaluated; the longitudinal acoustic (LA) mode is found to be the main contributor in monolayer SnS_2 while the transverse acoustic (TA) mode is the main contributor in monolayer $SnSe_2$. The size effects on lattice thermal conductivity are also discussed. Owing to their ultra low lattice thermal conductivity and high carrier mobility, monolayer SnS_2 and $SnSe_2$ are promising for thermoelectric applications.

2 Computational methods

All the density functional theory calculations are performed by adopting the Vienna Ab initio Simulation Package[33] with the projector augmented wave method.[34] The generalized gradient approximation in the form of Perdew–Burke–Ernzerhof[35] is used as an exchange correlation functional. The kinetic energy cutoff is set to 500 eV. The Monkhorst–Pack k-mesh of 15 × 15 × 1 is used and the structure is optimized until the largest Hellmann–Feynman force component on each atom is less than 0.001 eV Å^{-1}. The Heyd–Scuseria–Ernzerhof (HSE06) hybrid functional is used to calculate the band structure and carrier mobility. Phonopy code is used to calculate the phonon spectra, phonon group velocities, Grüneisen parameters, and harmonic force constants with a supercell of 6 × 6 × 1 using the finite displacement method.[1,36] Lattice thermal conductivity is calculated by solving the Boltzmann transport equation for phonons as implemented in the ShengBTE code.[37,38] The anharmonic force constants are obtained using a supercell of 5 × 5 × 1 including five nearest neighbors.

3 Results and discussion

3.1 Structure optimization and phonon spectra

The energetically and dynamically stable 1T phase of monolayer tin dichalcogenides (SnX_2) lies in the $P\bar{3}m1$ space group (No. 164), as shown in Fig. 1. The optimized lattice parameters of a hexagonal primitive unit cell are $a = b = 3.69$ Å for monolayer SnS_2 and $a = b = 3.86$ Å for monolayer $SnSe_2$. The lattice parameters are in good agreement with the previously reported values.[39,40] Monolayer SnX can be derived from the distorted tetrahedra of Sn(II) atoms with a lone pair. In this monolayer three Sn–X bonds form with two different bond lengths. However, monolayer SnX_2 is derived from the octahedral coordination of Sn(IV) to form a hexagonal structure.

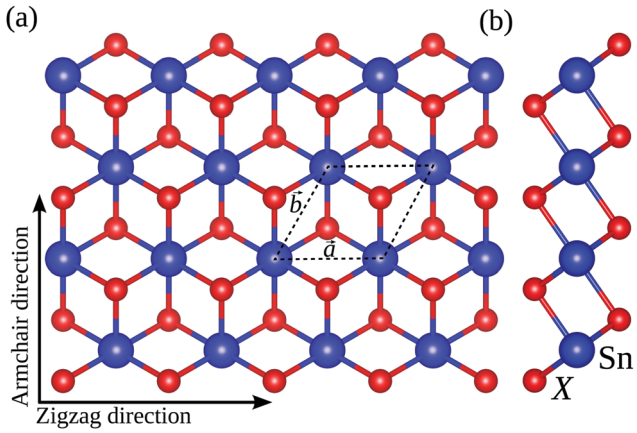

Fig. 1 (a) Top and (b) side views of the monolayer SnX_2 (X = S, Se). The dashed lines show the primitive unit cell (with lattice vectors $\vec{a}$ and $\vec{b}$).

The phonon spectra of the monolayer SnX_2 are shown in Fig. 2. The absence of imaginary frequencies in the phonon band structure for monolayer SnX_2 guarantees its dynamical stability. Among the total nine vibrational modes for the three atoms in a primitive unit cell, the lowest three modes are acoustic (LA, TA, and ZA (flexural acoustic mode)) modes and the other six modes with relatively high frequencies are the optical ones. The maximum frequency of vibration is 347.85 cm^{-1}

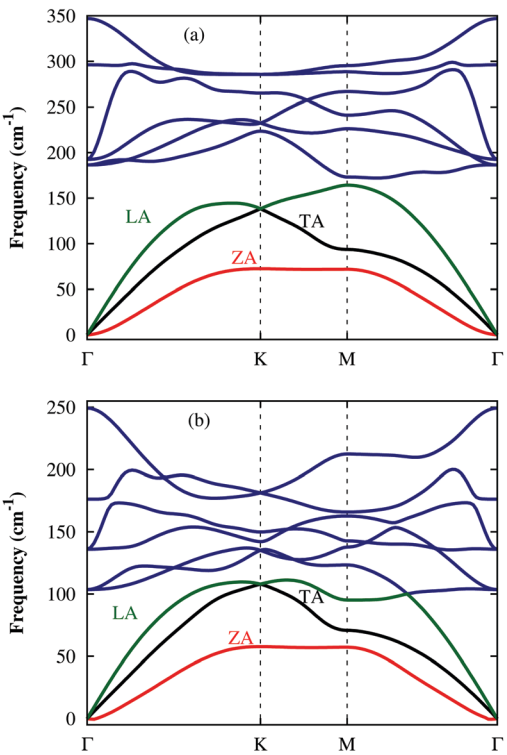

Fig. 2 Phonon band structure of (a) monolayer SnS_2 and (b) monolayer $SnSe_2$. The red, black, green, and blue lines represent the ZA, TA, LA, and optical modes, respectively.

Table 1 Percentage contribution of acoustic modes (ZA, TA, LA) and optical modes toward lattice thermal conductivity and total lattice thermal conductivity (κ_l) at room temperature, and the Debye temperature (Θ_D)

System	ZA (%)	TA (%)	LA (%)	Optical (%)	κ_l (W m^{-1} K^{-1})	Θ_D (K)
SnS_2	36.26	25.56	33.89	4.29	6.41	136.9
$SnSe_2$	29.85	32.32	29.53	8.30	3.82	107.8
SnS	27.07[22]	19.79[22]	25.97[22]	27.17[22]	3.21[22]	—
SnSe	31.39[22]	25.16[22]	14.90[22]	28.55[22]	2.95[22]	—
MoS_2	29.1[9]	30.4[9]	39.1[9]	1.4[9]	101[9]	262.3[8]
Graphene	76[47]	15[47]	8[47]	1[47]	3288[47]	2300[48]
Stanene	13.5[15]	26.9[15]	57.5[15]	2.1[15]	11.6[15]	72.5[15]
Silicene	38.98[16]	21.63[16]	20.97[16]	18.42[16]	27.72[16]	798.1[16]

for monolayer SnS_2 and 249.36 cm^{-1} for monolayer $SnSe_2$. The phonon band gap between the acoustic and optical modes for monolayer SnS_2 is larger than that for monolayer $SnSe_2$ because of the higher mass ratio of Sn to S than Sn to Se. The LA and TA modes are linear and the ZA mode is nearly quadratic at the gamma point. The phonon spectra of these monolayers are very similar, but the frequencies of monolayer $SnSe_2$ are slightly shifted downward compared to that of monolayer SnS_2 because of its larger reduced mass. Monolayer SnX_2 has higher phonon frequencies than monolayer SnX due to the difference in the oxidation state of Sn in both these cases, as reported in ref. 22. The optical bands in phonon dispersion of the monolayer SnX are dispersive, which significantly increases the contribution of these branches to the lattice thermal conductivity (see Table 1).

3.2 Phonon group velocities, Grüneisen parameters, and Debye temperatures

In order to understand the lattice thermal conductivity of the monolayer SnX_2, we explore the phonon-related properties such as phonon spectra, phonon group velocity, Grüneisen parameter, and the Debye temperature. Phonon group velocities are computed from the phonon spectra along the Γ–M and Γ–K directions, as shown in Fig. 3. The phonon group velocity of each mode is given by $v_k = \frac{\partial \omega_k(q)}{\partial q}$, where ω, k, and q represent the vibrational frequency, the vibrational mode index, and the wave vector respectively. The phonon group velocities of monolayer SnS_2 at low frequency limit are 1948 m s^{-1} in the ZA mode, 3222 m s^{-1} in the TA mode, and 5160 m s^{-1} in the LA mode. For monolayer $SnSe_2$ the group velocities are 1604 m s^{-1} in the ZA mode, 2514 m s^{-1} in the TA mode, and 4044 m s^{-1} in the LA mode. The phonon group velocity of monolayer SnX_2 in the LA mode is smaller than that of graphene[41] (22 000 m s^{-1}), phosphorene[42] (8640 m s^{-1}), and silicene[16] (9520 m s^{-1}), and larger than that of stanene[15] (3600 m s^{-1}) and monolayer MoS_2[19] (1108 m s^{-1}).

The Grüneisen parameter γ is calculated for each phonon mode in order to quantify the anharmonicity of monolayer SnX_2, as plotted in Fig. 4. The Grüneisen parameters are evaluated using the definition:[43]

$$\gamma_k(q) = -\frac{a_0}{\omega_k(q)}\frac{\partial \omega_k(q)}{\partial a}$$

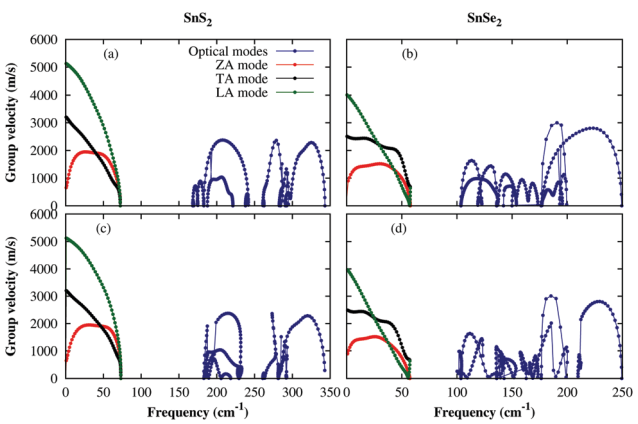

Fig. 3 Phonon group velocities along the (a) Γ–K, and (c) Γ–M directions for monolayer SnS_2 and along the (b) Γ–K, and (d) Γ–M directions for monolayer $SnSe_2$.

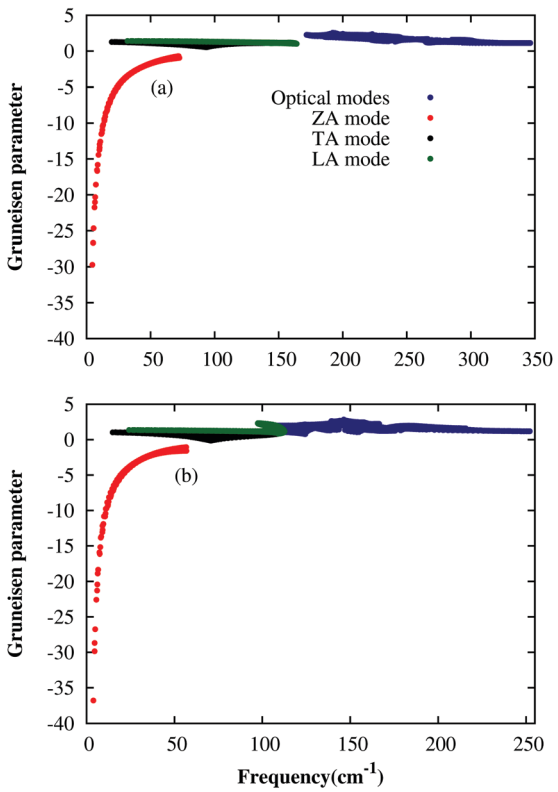

Fig. 4 Mode-dependent Grüneisen parameters of (a) monolayer SnS_2 and (b) monolayer $SnSe_2$.

where a_0 is the equilibrium lattice constant. Very large absolute values of the Grüneisen parameter are found at the long wavelength limit, which shows large phonon anharmonicity of monolayer SnX_2. The Slack's equation for lattice thermal conductivity[13] is:

$$\kappa_l = \frac{A\bar{M}\Theta_D\delta^{\frac{1}{3}}N^{\frac{1}{3}}}{\gamma^2 T}$$

where A is a constant and $\bar{M}$, Θ_D, δ, N, γ, and T are average atomic mass, Debye temperature, volume per atom, number of atoms per unit cell, Grüneisen parameter, and temperature, respectively. Therefore, strong anharmonicity (or large Grüneisen parameter) is required for low lattice thermal conductivity. Low Grüneisen parameter is reported for germanene, stanene, and silicene, and high for monolayer WS_2, MoS_2, and $MoSe_2$.[8,41] Finally, we calculate the Debye temperature (Θ_D) that is defined as[44]

$$\frac{1}{\Theta_D{}^3} = \frac{1}{3}\left(\frac{1}{\Theta_{ZA}{}^3} + \frac{1}{\Theta_{TA}{}^3} + \frac{1}{\Theta_{LA}{}^3}\right)$$

where $\Theta_i = \hbar\omega_i^{max}/k_B$ is the Debye temperature for each mode (i = ZA, TA, LA) and ω_i^{max} is the maximum frequency of the ith mode. The Debye temperatures for SnX_2 are listed in Table 1, which are smaller than those of graphene, silicene and monolayer MoS_2, and larger than that of stanene.[9,15,41] Small Debye temperatures for SnS_2 and $SnSe_2$ mean that many phonon modes are activated at room temperature, which leads to increasing phonon population and phonon scattering rate[45] to reduce the lattice thermal conductivity.

3.3 Lattice thermal conductivity (κ_l)

Lattice thermal conductivity is calculated using both the iterative and single mode relaxation time approximation (SMRTA) methods, as shown in Fig. 5. We find very low lattice thermal conductivity for monolayer SnS_2 (6.41 W m^{-1} K^{-1} for the iterative method and 5.44 W m^{-1} K^{-1} for the SMRTA method) and $SnSe_2$ (3.82 W m^{-1} K^{-1} for the iterative method and 3.23 W m^{-1} K^{-1} for the SMRTA method) at room temperature. The difference in the lattice thermal conductivity between the two methods for SnS_2 is larger than that for $SnSe_2$ because the SMRTA method is usually a good approximation for low thermal conducting materials. In the SMTRA method, the individual phonon mode is excited and has no memory of the initial phonon distribution. This approach only works when normal processes are dominated over the Umklapp processes. It is not a good approximation for high thermal conducting materials such as graphene or GaN. The iterative method solves the Boltzmann transport equation exactly and gives a fully converged value of the lattice thermal conductivity. It is equally applicable for high and low lattice thermal conducting materials.[46] The lattice thermal conductivities of the monolayer SnX_2 are compared with other well-known two-dimensional materials in Table 1. The low lattice thermal conductivities of the monolayer SnX_2 are due to their low phonon velocities, strong anharmonicity, and low Debye temperatures compared to other two-dimensional materials.

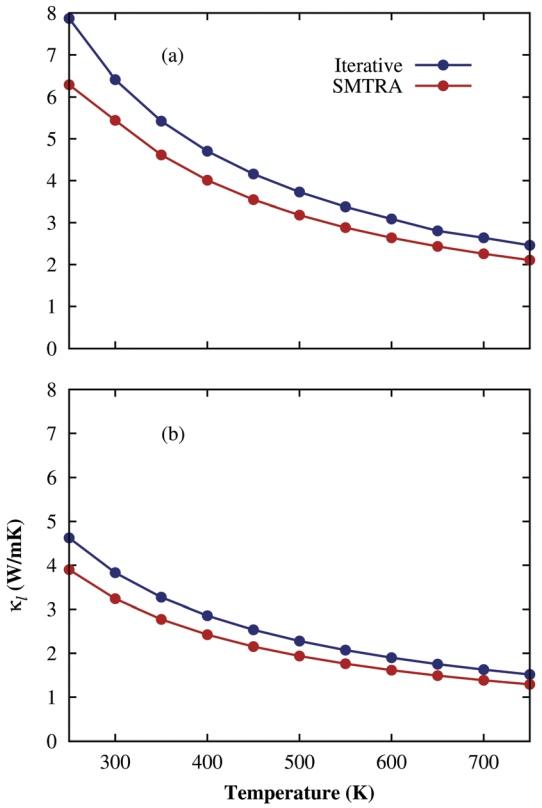

Fig. 5 Calculated lattice thermal conductivities as a function of temperature for the monolayer (a) SnS_2 and (b) $SnSe_2$.

Contributions of acoustic and optical modes to the lattice thermal conductivity are tabulated in Table 1. The contribution from the ZA mode of SnX_2 is smaller than that of graphene, because graphene has reflection symmetry which does not allow the ZA-mode anharmonic phonons to scatter. Approximately 60% contribution to the lattice thermal conductivity of monolayer SnX_2 comes from the TA and LA modes (unlike graphene) because of the strong anharmonic interactions. The contribution of SnX_2 is compared with well-known two-dimensional materials in Table 1.

The cumulative lattice thermal conductivity as a function of phonon mean free path (MFP, Λ) is plotted in Fig. 6. The cumulative lattice thermal conductivity shows the dependence of lattice thermal conductivity on the size of the sample and the lattice thermal conductivity reaches its saturation value when the size of the sample is equal to or larger than that for the maximal phonon MFPs (Λ_{max}). It also gives information regarding which phonon (long MFP or short MFP) contributes more to the lattice thermal conductivity. It is a very useful property in order to get information about how nanostructuring can decrease the lattice thermal conductivity.[49–51] Λ for monolayer SnS_2 is 486.2 nm and 278 nm for monolayer $SnSe_2$. The values of Λ_{max} of SnS_2 and $SnSe_2$ are very large, which means that nanostructuring can be effectively modulated by the lattice thermal conductivity. In order to find an important parameter

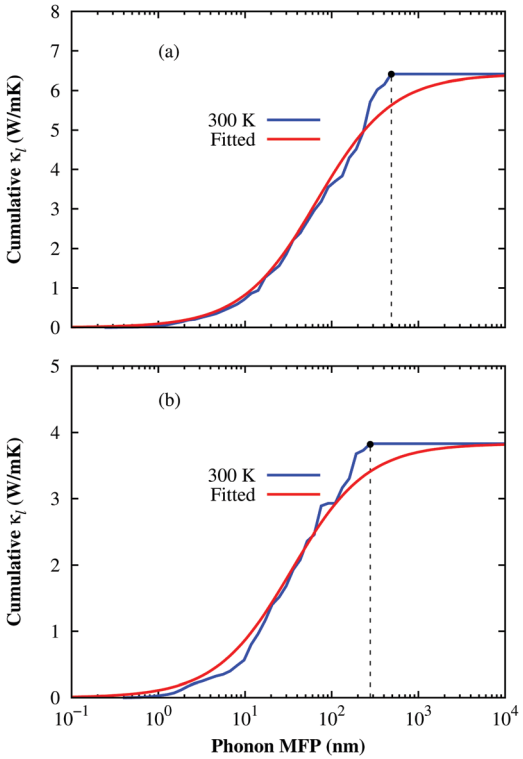

Fig. 6 The cumulative lattice thermal conductivity as a function of phonon MFP for (a) monolayer SnS_2 and (b) monolayer $SnSe_2$ at room temperature.

for designing nanostructuring, called the representative phonon MFP (Λ_0), the data are fitted to a single parametric function:[18,38]

$$\kappa_l(\Lambda \le \Lambda_{max}) = \frac{\kappa_{max}}{1 + \Lambda_0/\Lambda},$$

where κ_{max} is the maximal lattice thermal conductivity. The values of Λ_0 for monolayer SnS_2 and $SnSe_2$ are 67.7 nm and 34.1 nm, respectively.

3.4 Carrier mobility (μ)

Bardeen and Shockley proposed the deformation potential theory to evaluate the carrier mobility,[52] and the deformation potential theory has been extensively used to calculate the mobility of two-dimensional materials.[53–56] In this theory, the mobility of single layer material μ_{2D} is defined as

$$\mu_{2D} = \frac{e\hbar^3 C^{2D}}{k_B T m^* m_d E_1^2}$$

where T is temperature, $m^* = \hbar^2\left(\frac{d^2E}{dk^2}\right)$ is the effective mass obtained from the curvature of the band at the band edge whereas curvature $\left(\frac{d^2E}{dk^2}\right)$ is calculated by least squares fit to a quadratic function, and $m_d = \sqrt{m^*_{\Gamma-M} m^*_{M-K}}$ is the average effective mass. C^{2D} is the elastic constant defined by $C^{2D} = [\partial^2 E/\partial\delta^2]/A_0$, where E is the total energy after applying uniaxial strain ($\delta = \Delta l/l_0$) and A_0 is the area at equilibrium. The deformation potential

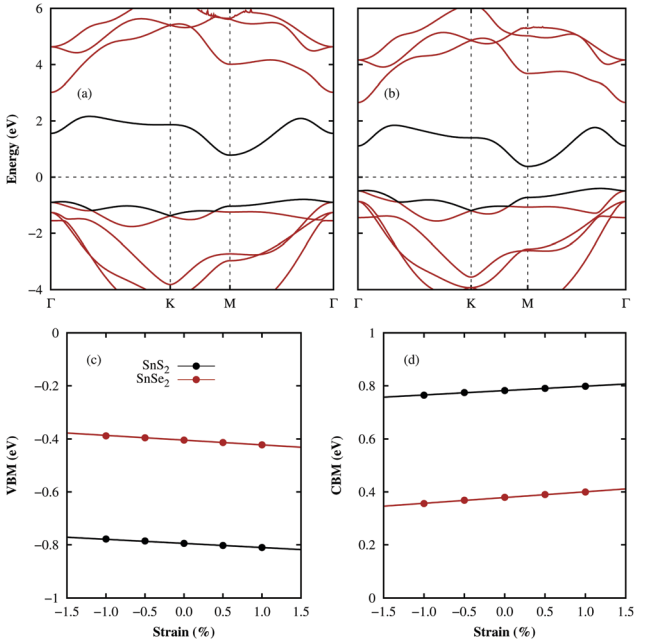

Fig. 7 Electronic band structure of monolayer (a) SnS_2 and (b) $SnSe_2$ along high symmetry points Γ, K, and M. (c) Shift in the valence band maxima under uniaxial strain and (d) shift in the conduction band minima under uniaxial strain.

constant E_1 is defined as $E_1 = \Delta V/\delta$, where ΔV represents the shift in band edge (conduction band minima or valence band maxima) by applying uniaxial strain δ. The calculated electronic band structures for the monolayer SnS_2 and $SnSe_2$ are shown in Fig. 7(a and b) with indirect band gaps of 2.38 and 1.39 eV, respectively. Band structure and carrier mobility calculations are based on the HSE06 method, a more accurate but computationally more expensive method. In both the monolayers, the conduction band maxima (CBM) are located at the M point and the valence band minima (VBM) are located between the Γ and M points. The VBM and CBM positions with respect to uniaxial strain are plotted in Fig. 7(c and d). The deformation potential constants are obtained by linear fitting of the CBM (for electrons) or VBM (for holes) *versus* the strain curve as listed in Table 2. The effective masses of an electron and a hole listed in Table 2 are calculated by fitting the bands near the CBM and VBM to quadratic functions. Our effective mass values are consistent with the previously reported ones.[57] The effective masses of the holes in the monolayer SnX_2 are heavier than those of the

Table 2 Effective mass ($m_{\Gamma-M}$*, m_{K-M}*), average effective mass (m_d), in-plane stiffness (C^{2D}), deformation constant (E_1), and mobility (μ) for holes and electrons in single layer SnX_2 at 300 K. The unit of effective masses is m_e

	Carrier	$m_{\Gamma-M}$*	m_{K-M}*	m_d	E_1 (eV)	μ (cm^2 V^{-1} s^{-1})	τ (fs)
SnS_2	Electron	0.73	0.30	0.46	−2.344	756.60	314.03
	Hole	−2.12	−0.40	0.92	−1.97	187.44	225.93
$SnSe_2$	Electron	0.71	0.31	0.47	−2.79	462.61	186.74
	Hole	−2.06	−0.39	0.89	−2.37	115.65	135.46

electrons due to the flatness of the valence band. The small effective masses of the electrons indicate that the electron mobility would be high. The elastic constants (C^{2D}) are calculated directly from the strain–stress relationship and the calculated values of C^{2D} for monolayers SnS_2 and $SnSe_2$ are 66.86 N m^{-1} and 56.32 N m^{-1}, respectively, and they are consistent with previous studies.[7,58] The monolayer SnS_2 has higher elastic constants compared to monolayer $SnSe_2$ due to the Sn–S bond being stronger than the Sn–Se bond.

The electronic properties of the monolayer SnX_2 are driven by carrier mobilities and strongly held by their effective masses. The carrier mobilities are determined by applying the standard two-dimensional model, the so-called acoustic phonon-limited mobility model in which acoustic phonon scattering is the fundamental process.[23,26,55] The carrier mobility and relaxation time ($\tau = \mu m^*/e$) for the electrons and holes of monolayer SnX_2 are computed on the basis of the calculated effective mass, elastic constant, and deformation potential constant as listed in Table 2. Predicted carrier mobilities of electrons and holes are highly asymmetric: a high mobility of 756.60 $cm^2 V^{-1} s^{-1}$ for electrons and 187.44 $cm^2 V^{-1} s^{-1}$ for holes in monolayer SnS_2. The electron carrier mobilities of the SnX_2 are higher than those of monolayer MoS_2 (60.32 $cm^2 V^{-1} s^{-1}$) and Ti_2CO_2 (611 $cm^2 V^{-1} s^{-1}$) because of the lower effective mass and lower deformation potential constant of monolayer SnX_2. It is lower than that for monolayer SnSe (1200 $cm^2 V^{-1} s^{-1}$) and phosphorene (1100 $cm^2 V^{-1} s^{-1}$).[23,26,55,59] Such large electron carrier mobilities grant n-type electronic properties to monolayer SnX_2 materials.

4 Conclusions

In conclusion, we have explored ultralow lattice thermal conductivity and high carrier mobility in monolayer SnS_2 and $SnSe_2$ using first principles calculations. In order to explain the ultralow lattice thermal conductivities, we have calculated the phonon spectra, phonon group velocities, Grüneisen parameters, and Debye temperatures. Monolayer $SnSe_2$ has lower lattice thermal conductivity than SnS_2 due to its low phonon group velocity, heavy mass of Se, strong anharmonicity, and low Debye temperature. The contribution of each vibrational mode to the lattice thermal conductivity is calculated and the size dependence of the lattice thermal conductivity is also discussed. The phonon MFPs for these materials are so large that phonon transport properties can be changed more efficiently by nanostructuring. The electron and hole mobility of monolayer $SnSe_2$ is higher than that of monolayer SnS_2 because of the low effective masses. The ultralow lattice thermal conductivity and high carrier mobility of monolayer SnS_2 and $SnSe_2$ suggest that they are good candidates for thermoelectric applications.

Acknowledgements

This work was supported by Basic Science Research Program (NRF-2014R1A2A1A11050893), Nano-Material Technology Development Program (NRF-2014M3A7B4049367), Basic Research Laboratory (NRF-2014R1A4A1071686), and Priority Research Center Program (2009-0093818) through the National Research Foundation of Korea funded by the Ministry of Science, ICT and Future Planning.

References

1 S. Baroni, S. de Gironcoli, A. Dal Corso and P. Giannozzi, *Rev. Mod. Phys.*, 2001, **73**, 515–562.
2 G. Wang, X. Shen, J. Yao and J. Park, *Carbon*, 2009, **47**, 2049–2053.
3 K. S. Novoselov, V. I. Fal'ko, L. Colombo, P. R. Gellert, M. G. Schwab and K. Kim, *Nat. Rev.*, 2012, **490**, 192–200.
4 Y. Xu, Z. Li and W. Duan, *Small*, 2014, **10**, 2182–2199.
5 A. Splendiani, L. Sun, Y. Zhang, T. Li, J. Kim, C.-Y. Chim, G. Galli and F. Wang, *Nano Lett.*, 2010, **10**, 1271–1275.
6 L. David, R. Bhandavat and G. Singh, *ACS Nano*, 2014, **8**, 1759–1770.
7 A. Samad, M. Noor-A-Alam and Y.-H. Shin, *J. Mater. Chem. A*, 2016, **4**, 14316–14323.
8 B. Peng, H. Zhang, H. Shao, Y. Xu, X. Zhang and H. Zhu, *RSC Adv.*, 2016, **6**, 5767–5773.
9 B. Peng, H. Zhang, H. Shao, Y. Xu, X. Zhang and H. Zhu, *Ann. Phys.*, 2016, **528**, 504–511.
10 A. Samad, A. Shafique and Y.-H. Shin, *Nanotechnology*, 2017, **28**, 175401.
11 J. R. Szczech, J. M. Higgins and S. Jin, *J. Mater. Chem.*, 2011, **21**, 4037–4055.
12 S. Hao, F. Shi, V. P. Dravid, M. G. Kanatzidis and C. Wolverton, *Chem. Mater.*, 2016, **28**, 3218–3226.
13 G. A. Slack, *J. Phys. Chem. Solids*, 1973, **34**, 321–335.
14 B. D. Kong, S. Paul, M. B. Nardelli and K. W. Kim, *Phys. Rev. B: Condens. Matter Mater. Phys.*, 2009, 033406.
15 B. Peng, H. Zhang, H. Shao, Y. Xu, X. Zhang and H. Zhu, *Sci. Rep.*, 2016, **6**, 20225.
16 B. Peng, H. Zhang, H. Shao, Y. Xu, R. Zhang, H. Lu, D. W. Zhang and H. Zhu, *ACS Appl. Mater. Interfaces*, 2016, **8**, 20977–20985.
17 A. Shafique and Y.-H. Shin, *Sci. Rep.*, 2017, **7**, 506.
18 G. Qin, Q.-B. Yan, Z. Qin, S.-Y. Yue, M. Hu and G. Su, *Phys. Chem. Chem. Phys.*, 2015, **17**, 4854–4858.
19 Y. Cai, J. Lan, G. Zhang and Y.-W. Zhang, *Phys. Rev. B: Condens. Matter Mater. Phys.*, 2014, **89**, 035438.
20 X. Gu and R. Yang, *Appl. Phys. Lett.*, 2014, **105**, 131903.
21 W.-X. Zhou and K.-Q. Chen, *Sci. Rep.*, 2015, **5**, 15070.
22 G. Qin, Z. Qin, W.-Z. Fang, L.-C. Zhang, S.-Y. Yue, Q.-B. Yan, M. Hu and G. Su, *Nanoscale*, 2016, **8**, 11306–11319.
23 Y. Cai, G. Zhang and Y.-W. Zhang, *J. Am. Chem. Soc.*, 2014, **136**, 6269–6275.
24 X.-B. Li, P. Guo, Y.-N. Zhang, R.-F. Peng, H. Zhang and L.-M. Liu, *J. Mater. Chem. C*, 2015, **3**, 6284–6290.
25 Y. Aierken, D. Cakir and F. M. Peeters, *Phys. Chem. Chem. Phys.*, 2016, **18**, 14434–14441.
26 L.-C. Zhang, G. Qin, W.-Z. Fang, H.-J. Cui, Q.-R. Zheng, Q.-B. Yan and G. Su, *Sci. Rep.*, 2016, **6**, 19830.

27 F. Li, X. Liu, Y. Wang and Y. Li, *J. Mater. Chem. C*, 2016, **4**, 2155–2159.
28 X. Zhou, L. Gan, W. Tian, Q. Zhang, S. Jin, H. Li, Y. Bando, D. Golberg and T. Zhai, *Adv. Mater.*, 2015, **27**, 8035–8041.
29 H. Wang, Y. Gao and G. Liu, *RSC Adv.*, 2017, **7**, 8098–8105.
30 Y. Ding, B. Xiao, G. Tang and J. Hong, *J. Phys. Chem. C*, 2017, **121**, 225–236.
31 A. N. Gandi and U. Schwingenschlogl, *EPL*, 2016, **113**, 36002.
32 S. Kumar and U. Schwingenschlogl, *Chem. Mater.*, 2015, **27**, 1278–1284.
33 G. Kresse and J. Furthmüller, *Phys. Rev. B: Condens. Matter Mater. Phys.*, 1996, **54**, 11169–11186.
34 G. Kresse and D. Joubert, *Phys. Rev. B: Condens. Matter Mater. Phys.*, 1999, **59**, 1758.
35 J. P. Perdew, K. Burke and M. Ernzerhof, *Phys. Rev. Lett.*, 1996, **77**, 3865–3868.
36 A. Togo, F. Oba and I. Tanaka, *Phys. Rev. B: Condens. Matter Mater. Phys.*, 2008, **78**, 134106.
37 W. Li, L. Lindsay, D. A. Broido, D. A. Stewart and N. Mingo, *Phys. Rev. B: Condens. Matter Mater. Phys.*, 2012, **86**, 174307.
38 W. Li, J. Carrete, N. A. Katcho and N. Mingo, *Comput. Phys. Commun.*, 2014, **185**, 1747–1758.
39 H. L. Zhuang and R. G. Hennig, *Phys. Rev. B: Condens. Matter Mater. Phys.*, 2013, **88**, 115314.
40 Y. Huang, D. Zhou, X. Chen, H. Liu, C. Wang and S. Wang, *ChemPhysChem*, 2016, **17**, 375–379.
41 B. Peng, H. Zhang, H. Shao, Y. Xu and H. Zhu, *Phys. Rev. B*, 2016, **94**, 245420.
42 T.-H. Liu and C.-C. Chang, *Nanoscale*, 2015, **7**, 10648–10654.
43 N. Mounet and N. Marzari, *Phys. Rev. B: Condens. Matter Mater. Phys.*, 2005, **71**, 205214.
44 D. T. Morelli and J. P. Heremans, *Appl. Phys. Lett.*, 2002, **81**, 5126–5128.
45 T. Nakashima and Y. Umakoshi, *Philos. Mag. Lett.*, 1992, **66**, 317–321.
46 G. Fugallo, M. Lazzeri, L. Paulatto and F. Mauri, *Phys. Rev. B: Condens. Matter Mater. Phys.*, 2013, **88**, 045430.
47 L. Lindsay, W. Li, J. Carrete, N. Mingo, D. A. Broido and T. L. Reinecke, *Phys. Rev. B: Condens. Matter Mater. Phys.*, 2014, **89**, 155426.
48 D. K. Efetov and P. Kim, *Phys. Rev. Lett.*, 2010, **105**, 256805.
49 A. Balandin and K. L. Wang, *Phys. Rev. B: Condens. Matter Mater. Phys.*, 1998, **58**, 1544–1549.
50 D. Aketo, T. Shiga and J. Shiomi, *Appl. Phys. Lett.*, 2014, **105**, 131901.
51 G. Fugallo, A. Cepellotti, L. Paulatto, M. Lazzeri, N. Marzari and F. Mauri, *Nano Lett.*, 2014, **14**, 6109–6114.
52 J. Bardeen and W. Shockley, *Phys. Rev.*, 1950, **80**, 72–80.
53 S. Bruzzone and G. Fiori, *Appl. Phys. Lett.*, 2011, **99**, 222108.
54 J. Xi, M. Long, L. Tang, D. Wang and Z. Shuai, *Nanoscale*, 2012, **4**, 4348–4369.
55 J. Qiao, X. Kong, Z.-X. Hu, F. Yang and W. Ji, *Nat. Commun.*, 2014, **5**, 4475.
56 Y. Xu, J. Dai and X. C. Zeng, *J. Phys. Chem. Lett.*, 2016, **7**, 302–307.
57 J. M. Gonzalez and I. I. Oleynik, *Phys. Rev. B*, 2016, **94**, 125443.
58 D. M. Guzman and A. Strachan, *J. Appl. Phys.*, 2014, **115**, 243701.
59 X. Zhang, X. Zhao, D. Wu, Y. Jing and Z. Zhou, *Nanoscale*, 2015, **7**, 16020–16025.